nature portfolio

https://doi.org/10.1038/s41586-022-05268-x

Supplementary information

Surface reaction for efficient and stable inverted perovskite solar cells

In the format provided by the authors and unedited

Supplementary Information

Surface reaction for efficient and stable inverted perovskite solar cells

Qi Jiang,[1†] Jinhui Tong,[1†] Yeming Xian,[2] Ross A. Kerner,[1] Sean P. Dunfield,[3,4] Chuanxiao Xiao,[4] Rebecca A. Scheidt,[1] Darius Kuciauskas,[1] Xiaoming Wang,[2] Matthew P. Hautzinger,[1] Robert Tirawat,[1] Matthew C. Beard,[1] David P. Fenning,[3] Joseph J. Berry,[4,5,6] Bryon W. Larson,[1] Yanfa Yan,[2*] Kai Zhu[1*]

[1] Chemistry and Nanoscience Center, National Renewable Energy Laboratory, Golden, CO 80401, USA

[2] Department of Physics and Astronomy and Wright Center for Photovoltaics Innovation and Commercialization, University of Toledo, Toledo, OH 43606, USA

[3] Department of NanoEngineering, University of California San Diego, La Jolla, CA 92093, USA

[4] Materials Science Center, National Renewable Energy Laboratory, Golden, CO 80401, USA

[5] Renewable and Sustainable Energy Institute, University of Colorado Boulder, Boulder, CO 80309, USA

[6] Department of Physics, University of Colorado Boulder, Boulder, CO 80309, USA

* Corresponding authors: Yanfa.Yan@utoledo.edu (Y.Y.); Kai.Zhu@nrel.gov (K.Z.)

† These authors contributed equally to this work.

Supplementary Note 1. Condensation reaction from perovskite surface treatment

The general condensation reaction was observed and confirmed for methylamine as shown in ref. [1] and [2]. From their ^{1}H-NMR results, it is unambiguous that a metathesis-like reaction occurs between formamidinium and methylamine, and the reaction products N-methyl formamidinium (MFA^{+}) and N,N'-dimethyl formamidinium ($DMFA^{+}$) are easily identified by proton NMR. This reaction should be general to other "simple" primary amines as well.

In the scheme in **Supplementary Fig. 1**, we show **1)** the reaction with FA^{+} where the amine molecule is methylamine, as discussed in ref. 6; **2)** the generalized reaction between FA^{+} and a primary amine molecule with side group **R**; and **3)** the reaction with FA^{+} where the amine is 3-(Aminomethyl)pyridine (3-APy, where Py denotes pyridine). To facilitate our discussion, we also refer to the main reaction product as MPyFA (N-(3-methylpyridine)formamidinium); the other reaction product is NH_3 (ammonia). The key takeaway from the Scheme below is that in all cases (ref. 6, the general chemical mechanism, and our study), an ammonia condensation reaction takes place between a primary amine and FA^{+}.

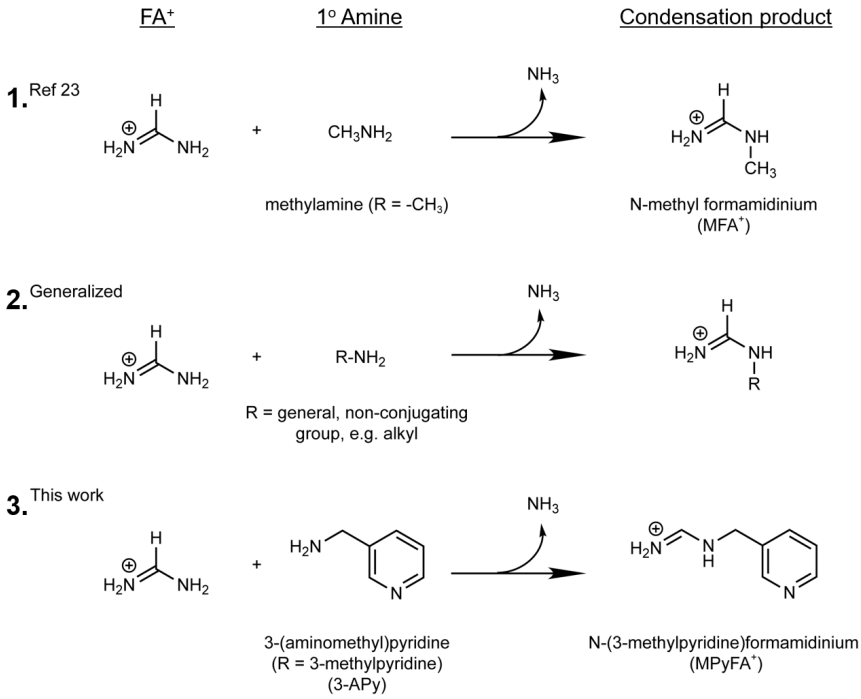

Supplementary Fig. 1. Condensation reaction schemes. Scheme **1** illustrates the reported condensation reaction from ref. 1 (ref. 23 in the main text), showing the reaction between FA and methylamine resulting in MFA and release of ammonia (NH_3). Scheme **2** shows the generalized reaction. Scheme **3** shows the analog condensation reaction of FA and 3-APy in this work.

We performed ^{1}H-NMR to support our proposed reaction products for 3-APy. **Supplementary Fig. 2** shows the spectra of 3-APy, MAI + 3-APy, and FAI + 3-APy in DMSO-d6. It is clear from these data that FA^{+} and 3-APy react to form a unique product, whereas MAI and 3-APy simply exchange acidic NH protons. Our results show that a reaction has nearly fully occurred between FA^{+} and 3-APy within 10 minutes at room temperature, which does not rule out a faster reaction time, as this is the minimum amount of time it takes to go from sample preparation to completing the measurement.

Before concluding these data as direct evidence for our proposed surface mechanism, we need quantitative integration proving a 1:2:3 H-shift ratio of the protons involved in the condensation reaction product (MPyFA, see Scheme above). Unfortunately, clean integration of chemical shifts ascribed to these protons is complicated by the FA "formic" CH peak and broad NH proton peaks overlapping with the MPyFA formic proton. Additionally, the NH_3 chemical shifts are un-resolvable at this pH and temperature given how rapidly proton exchange is occurring.

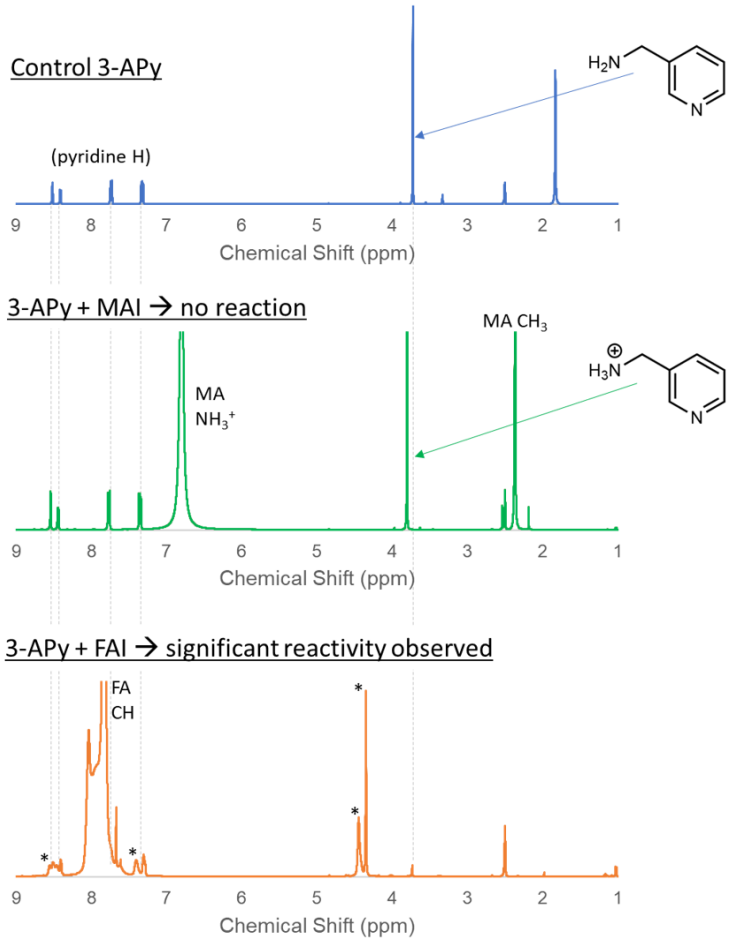

Supplementary Fig. 2. ^{1}H-NMR spectra of (top to bottom) 3-APy (0.01 M), MAI with 3-APy (0.1 M and 0.01 M, respectively), and FAI with 3-APy (0.1 M and 0.01 M, respectively). Reactions resulting in large proton peak shifts or new peaks (marked with *) are only observed for FAI + 3-APy. 400 MHz in DMSO-d6 stored on sieves (ultra-dry).

To overcome the inability to resolve NH_3 shifts under these conditions, as well as sharpen each fingerprint proton shift to allow for clean integration, we employed an HI spiking technique following the protocol published elsewhere[3]. NH_3/NH_4^+ would otherwise be invisible to ^{1}H-NMR due to rapid acidic proton exchange enabled by the addition of amine (3-APy). In doing so, we force HI to protonate all species in solution, including NH_3, to form NH_4^+, so it can then be detected due to reduced proton exchange rate.

The results of HI spiking FAI (0.1 M) + 3-APy (0.01 M) in DMSO-d6 are shown in **Supplementary Fig. 3**. The peaks are highly split with better separations, and NH_4^+ is clearly visible in large amounts, proving the condensation reaction. The integration for our assignment of the MPyFA formic CH, -CH_2-, and NH_4^+ hydrogens are shown at the top of the figure. These

results quantitatively agree with the expected ratio of $CH:CH_2:NH_4$ = 1:2:4 to within expected uncertainty of this measurement (note the ammonia H ratio is not 3 because it is protonated by HI).

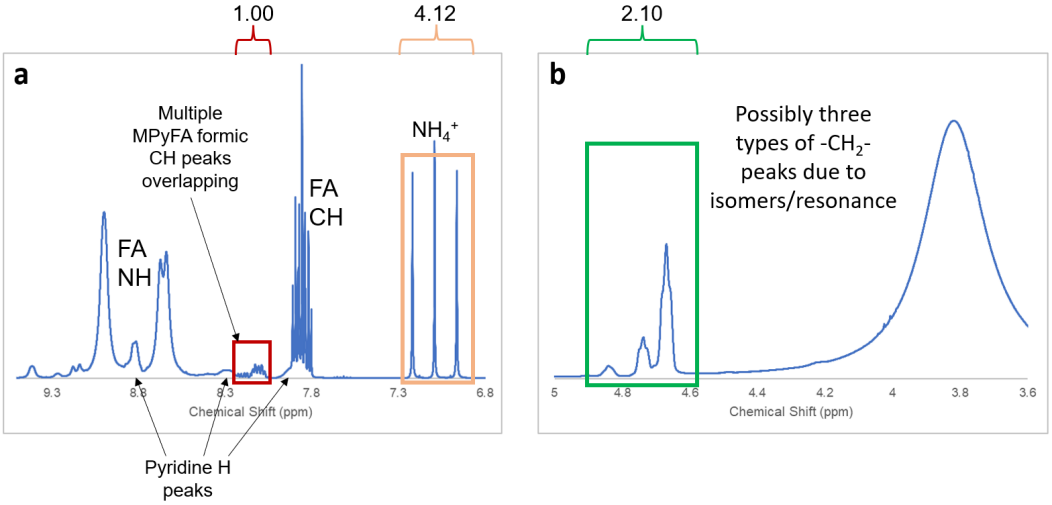

Supplementary Fig. 3. (**a**) Downfield and (**b**) upfield ^{1}H-NMR of the FAI + 3-APy after spiking with 2 µL HI. The "formic" C-H protons in the products are identified slight downfield from the FA CH, and display the similar fine-splittings as the FA CH. The NH_4^+ is visible as a triplet with ~51 Hz splitting centered near 7.1 ppm. The methylene -CH_2- protons corresponding to different isomers for the MPyFA product are located 4.6-4.9 ppm in (b). 400 MHz in DMSO-d6.

For reference, and to justify our integration of three different -CH_2- peaks, the three possible isomers of MPyFA are depicted in **Supplementary Fig. 4**, acknowledging both the possibility for resonance and isomers to manifest in the spectra when the proton exchange rate is negligible.

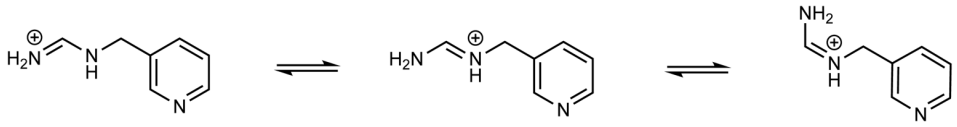

Supplementary Fig. 4. Different resonance structures and isomers of the 3-MPyFA condensation product that can contribute to three different -CH_2- peaks anticipated for the methylene C.

Finally, we characterized a set of samples to check for the unlikely event of a reaction between FA^+ and the pyridine (Py) nitrogen, i.e. – investigate the possibility of chemistries occurring besides the ammonia condensation reaction we propose. As shown in **Supplementary**

Fig. 5, the peaks for pyridine in the presence of excess FAI are unchanged from the control, demonstrating the amine nitrogen is the reactive group toward the FA^+ molecule.

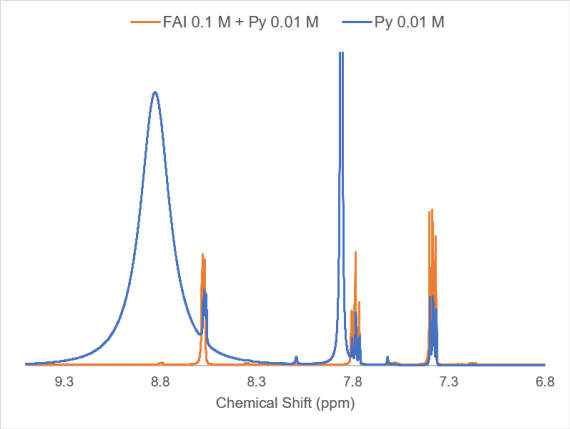

Supplementary Fig. 5. Downfield ^{1}H-NMR spectra of pyridine (Py) control (0.01 M) and Py with FAI (0.1 M) showing no reaction. 400 MHz in DMSO-d6.

We also conducted electrospray ionization mass spectrometry (ESI-MS) of a sample of FAI (0.1 M) + 3-APy (0.02 M), and detected a major peak at 136.087 m/z, which exactly matches the molecular mass of the MPyFA compound (136.087 amu). The results are shown in **Supplementary Fig. 6**.

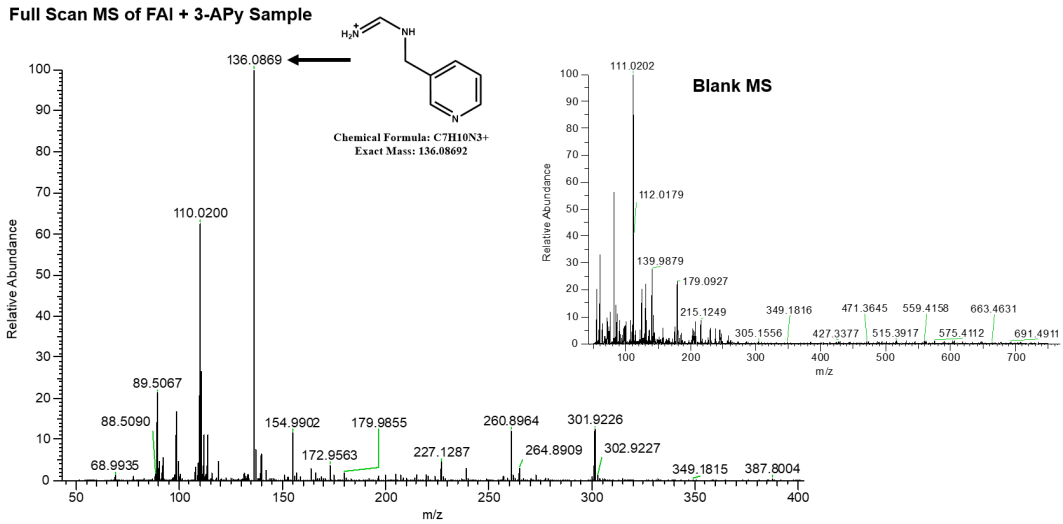

Supplementary Fig. 6. Electrospray ionization mass spectrometry (ESI-MS) of a sample of FAI (0.1 M) + 3-APy (0.02 M).

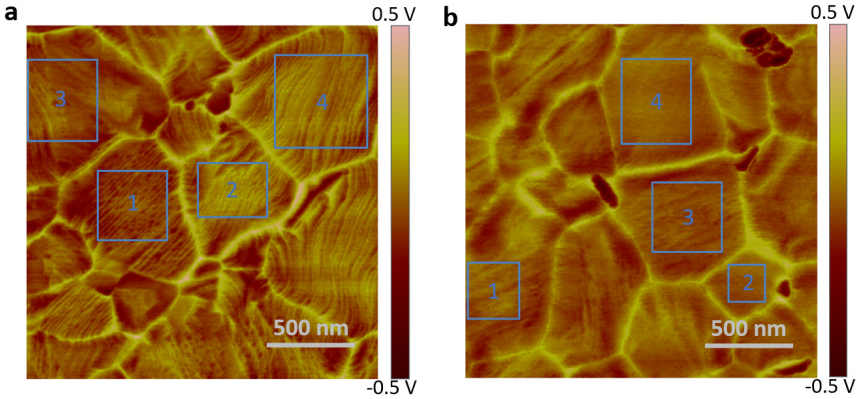

Supplementary Fig. 7. Comparison of KPFM surface potential variations. (**a**) Sample without surface treatment. The root-mean-square (RMS) roughness values for four regions (indicated) are (1) 41.5 mV, (2) 48.0 mV, (3) 38.5 mV, and (4) 41.8 mV. (**b**) Sample with 3-APy surface treatment. The RMS roughness values for four regions (indicated) are (1) 26.8 mV, (2) 13.1 mV, (3) 22.2 mV, and (4) 18.6 mV.

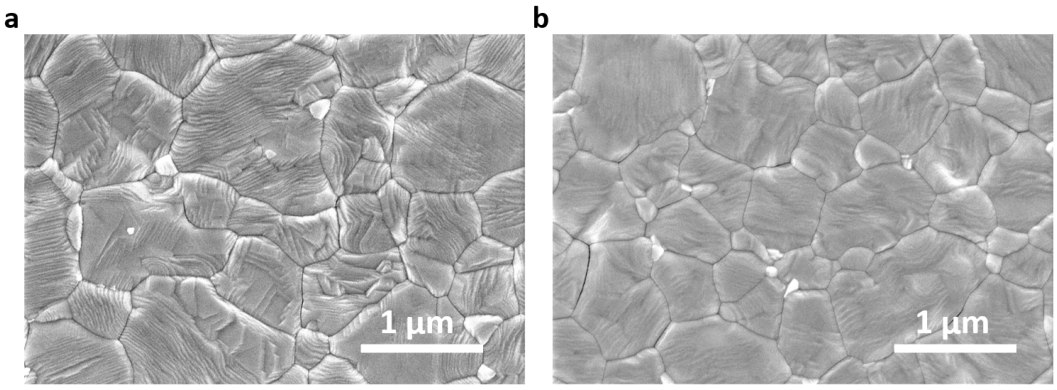

Supplementary Fig. 8. Scanning electron microscopy (SEM) images of perovskite surface before (**a**) and after (**b**) 3-APy treatment. It is clear to see the smoother surface after 3-APy treatment.

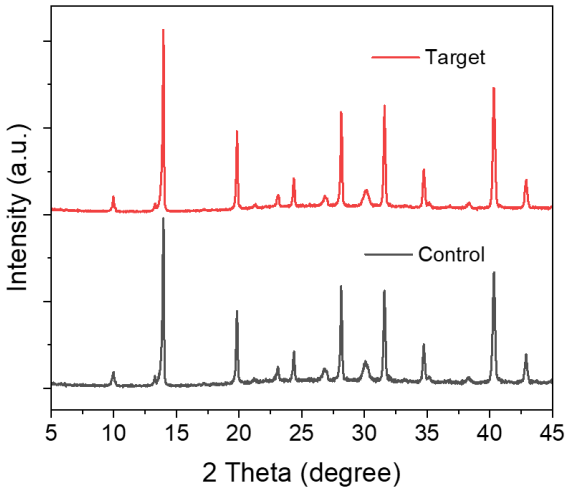

Supplementary Fig. 9. X-ray diffraction (XRD) comparison of the perovskite films without (control) and with (target) 3-APy treatment.

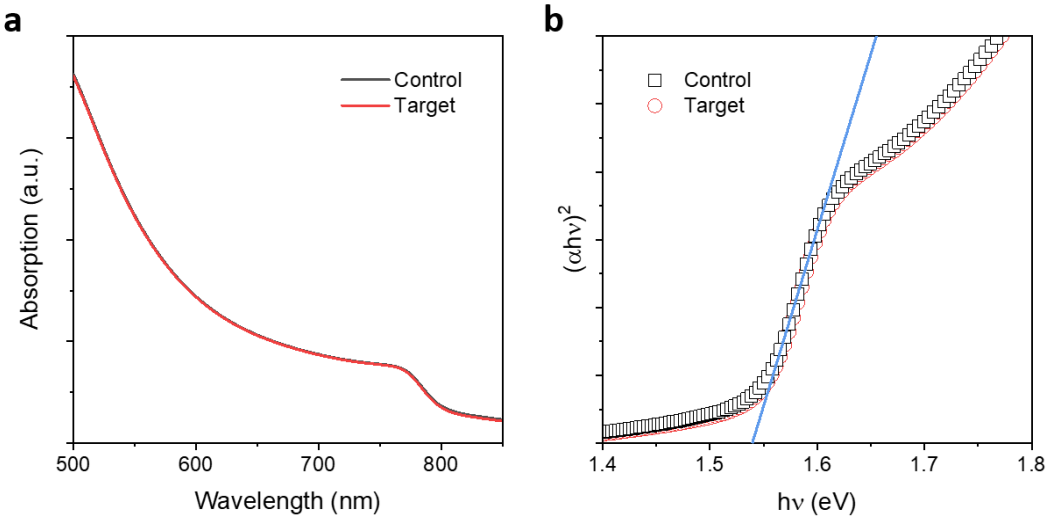

Supplementary Fig. 10. Ultraviolet-visible (UV-vis) absorption spectra (**a**) and the corresponding Tauc analyses (**b**) of perovskite films without (control) and with (target) 3-APy treatment. The perovskite bandgap was about 1.53 eV.

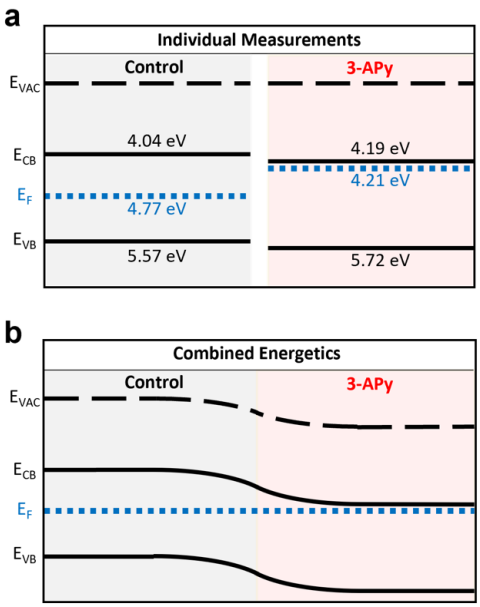

Supplementary Fig. 11. Schematics of energy level diagram. (**a**) Individual measurements of energy levels of perovskite films without (control) and with 3-APy treatment (3-APy), and (**b**) the corresponding band-bending schematics.

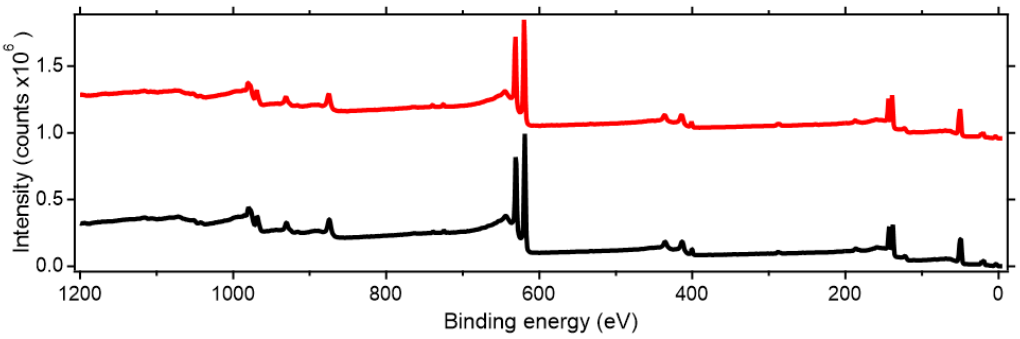

Supplementary Fig. 12. X-ray photoelectron spectroscopy (XPS) survey spectra of perovskite film without 3-APy (black) and with 3-APy (red).

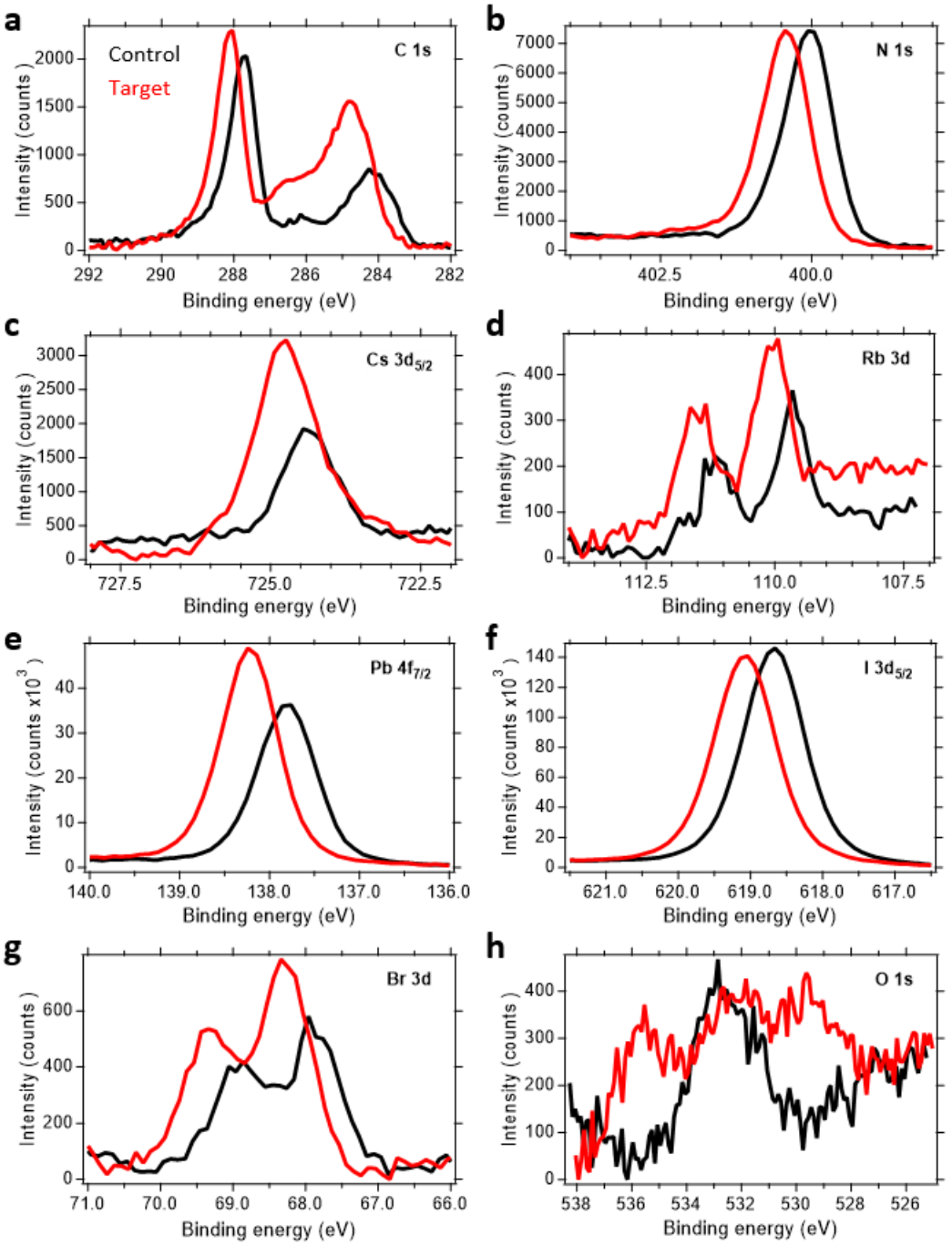

Supplementary Fig. 13. High-resolution XPS core-level spectra for all elements identified in the survey scan.

	Br %	Cs %	C %	I %	N %	O %	Pb %	Rb %	Pb:I	N:I	C:I
Control	1.3	0.4	19.1	42.3	22.8	1.3	12.4	0.4	0.29	0.54	0.45
Additive	1.6	0.9	25.5	36.4	20.6	0.2	14.4	0.5	0.39	0.57	0.70

Supplementary Fig. 14. Composition and ratios derived from the high-resolution core-level scans.

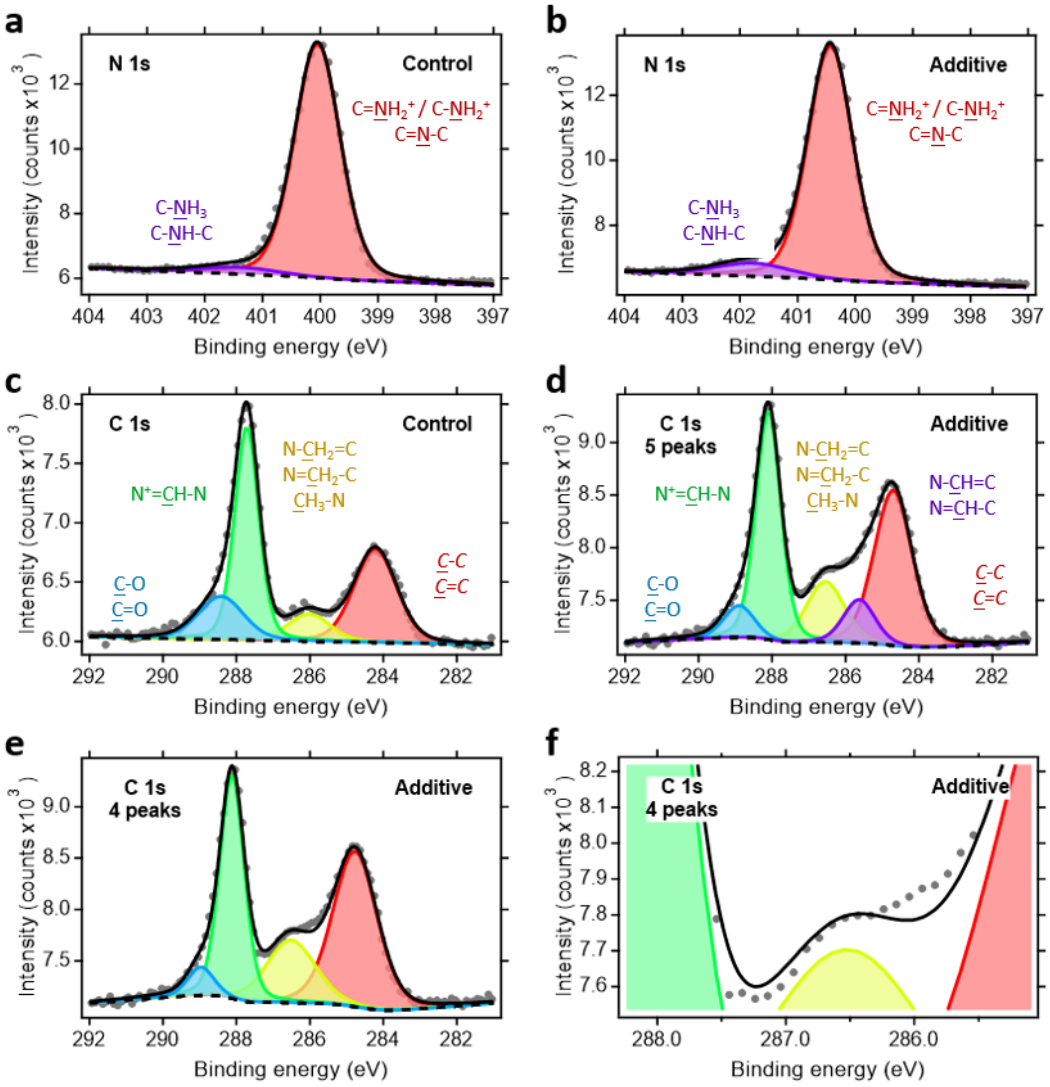

Supplementary Fig. 15. XPS core-level spectral fits for N 1s (**a–b**) and C 1s (**c–d**), plus an additional fitting attempt utilizing only four peaks (**e**) with its variance from the best fit line (**f**). As can be seen, the control sample's C 1s spectra can be easily fit with four peaks, but the 3-APy-treated sample requires a fifth peak. For all fits, the full width half maximum (FWHM) was constrained between 0.7 and 1.5 eV. Relative peak location constraints for the N 1s are N_1 = x and N_2 = x + 1.35 to 1.45 eV. Relative peak location constraints for C 1s are C_1 = x, C_2 = x + 1.75 to 1.85 eV, C_3 = x + 3.3 to 3.5 eV, and C_4 = x + 4.2 to 4.3 eV. For **d**, a fifth peak was added at C_5 = x + 0.85 to 0.95. For **e/f**, C_2 constraints in FWHM and position were removed.

Supplementary Note 2. Transient reflectance (TR) analysis

TR measurements were performed at 400, 600, and 700 nm excitation. By using various wavelengths for excitation, we are able to excite different volumes of the film due to changes in the absorption coefficient of the material. This means that pump wavelengths with higher photon energies (such as 400 nm) will cause a greater initial build-up of photogenerated charge carriers at the surface of the film than pump wavelengths with lower photon energies (such as 700 nm).

The distribution of photogenerated charge carriers can be well described using a one-dimensional diffusion model (**Equation S1**), which allows for a quantitative analysis of the photogenerated carrier population over time and at different film depths. The one-dimensional diffusion model shown below was used where $N(x,t)$ is the carrier density as a function of film depth (x) over time (t), τ_B is the lifetime of photogenerated charge carriers in the bulk, and D is the ambipolar diffusion coefficient of charge carriers in the film.

$$\frac{\partial N(x,t)}{\partial t} = D\frac{\partial^2 N(x,t)}{\partial x^2} - \frac{N(x,t)}{\tau_B} \quad \text{(S1)}$$

By assuming that the initial carrier generation happens instantaneously and within the time resolution of the pump excitation pulse, the initial carrier concentration at the surface of the film can be found using

$$N_0 = \alpha(1-R)J_0 \quad \text{(S2)}$$

where N_0 is the initial carrier density, α is the absorption coefficient at the chosen pump wavelength, R is the reflectance of the pump, and J_0 is the carrier density (calculated by the measured power output and measured spot size of the excitation pulse).

To solve the diffusion model, boundary conditions were set with the following conditions:

$$\left.\frac{\partial N(x,t)}{\partial t}\right|_{x=0} = \frac{SRV}{D}N(0,t) \text{ and } \left.\frac{\partial N(x,t)}{\partial t}\right|_{x=M} = \frac{SRV}{D}N(M,t) \quad \text{(S3)}$$

where M is the film thickness and SRV is the surface recombination velocity. The assumption was made that the SRV at the front and back sides of the film do not vary significantly, which has been

shown to be a valid assumption in previous reports. Additionally, the bulk recombination is considered to be negligible in the time window of the experiment (2.5 ns) since the bulk recombination typically occurs on a much longer time scale (>5 ns). While the film thickness is a known value, this system of equations cannot be solved analytically and must be solved using a backward finite difference method. By using the numerical solution $N(0,t)$, the TR kinetic traces (**Figs. 3a, b**) at the various pump wavelengths used are modeled with a global fit method which utilizes the above diffusion model and boundary conditions.

Supplementary Note 3. External radiative efficiency (ERE) measurement and analysis

PL emission was measured using 632.8-nm excitation (HeNe laser). To calculate an excitation fluence (in photons $cm^{-2}s^{-1}$)), the excitation beam size was determined with a CCD camera beam profiler (Thorlabs BC106N-VIS/M). We assumed that 1-sun equivalent fluence for our 1.53-eV absorber is 1.73×10^{17} photons $cm^{-2}s^{-1}$, and we adjusted the excitation fluence to this level. To measure PL emission spectra, Princeton Instruments HRS300 spectrograph with dual Si CCD (Pixis F100) and InGaAs (PyLoN IR) detectors was used. To correct spectral responses of both detectors, commercial calibration sources (IntelliCal for vis and IR ranges, Princeton Instruments) were placed at the sample position. Corrected PL emission spectra measured with two detectors were identical at 1.30-1.38 eV, confirming small band tails for control and target solar cells. Spectral integration at 1.30-1.90 eV was used to determine integrated PL intensity, and integrated PL emission intensity is plotted vs. excitation fluence in the inset of **Fig. 3d**. To report PL emission spectra in absolute units (photons $cm^{-2}eV^{-1}s^{-1}$), we used the same setup to measure excitation laser light scattering from reflectance standards (2%, 5%, and 99%, LabSphere Inc). We normalized PL spectra using the data where reflectance values were known, and in this way obtained absolute PL emission spectra (**Fig. 3d**).

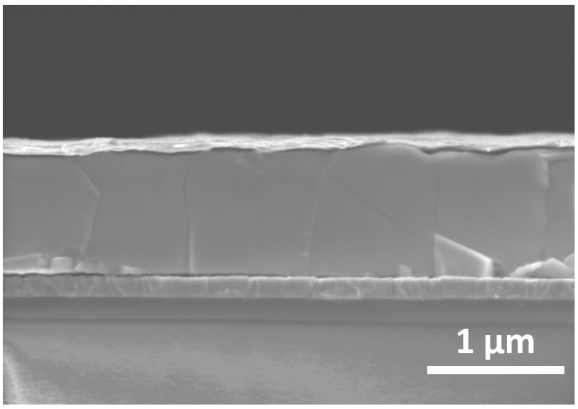

Supplementary Fig. 16. Cross-sectional SEM image of the p-i-n device with a typical device stack of glass/ITO/MeO-2PACZ/$Rb_{0.05}Cs_{0.05}MA_{0.05}FA_{0.85}Pb(I_{0.95}Br_{0.05})_3$/3-APy/LiF/$C_{60}$/BCP/Ag. The thickness of the perovskite layer is about 860 nm.

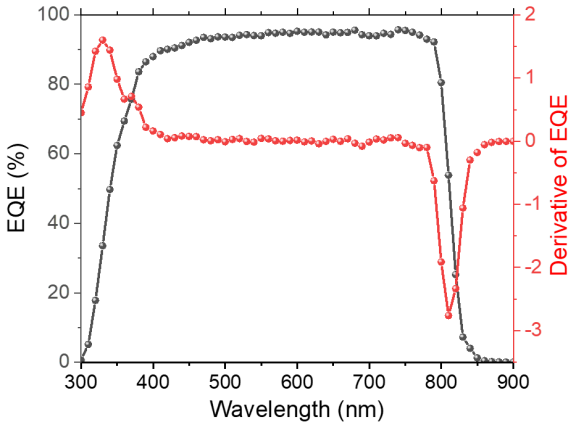

Supplementary Fig. 17. Analysis of perovskite bandgap from the external quantum efficiency (EQE) spectrum by taking its derivative spectrum. The bandgap was estimated to be about 1.53 eV.

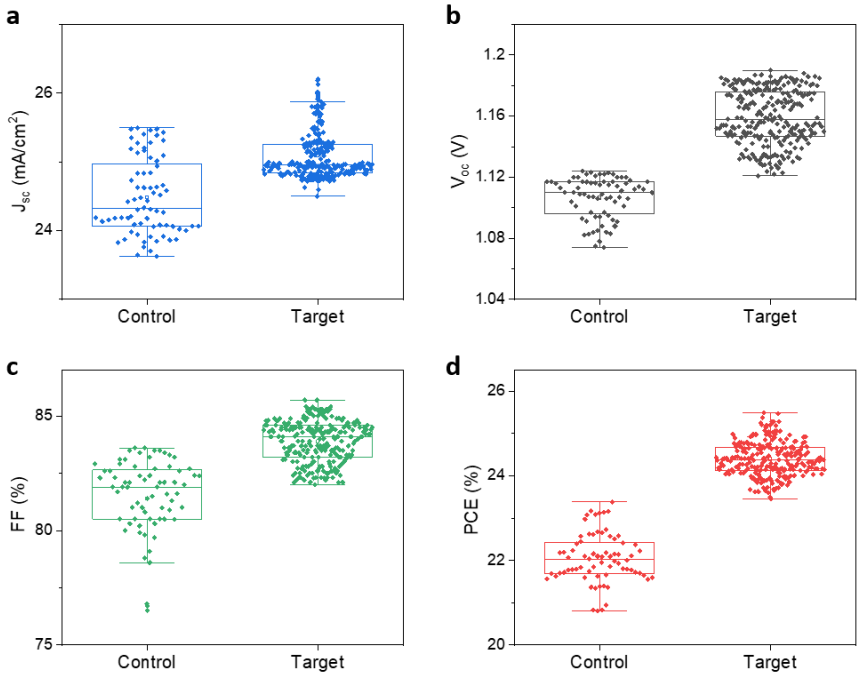

Supplementary Fig. 18. Statistical comparison of PV parameters of p-i-n devices based on perovskite films without (control) and with (target) 3-APy treatment. Plots of the box chart graphs containing the mean value, maximum/minimum values, and 25%-to-75%-region data of short-circuit current density (J_{sc}) (**a**), open-circuit voltage (V_{oc}) (**b**), fill factor (FF) (**c**), and power conversion efficiency (PCE) (**d**), based on 72 control and 246 target devices.

a

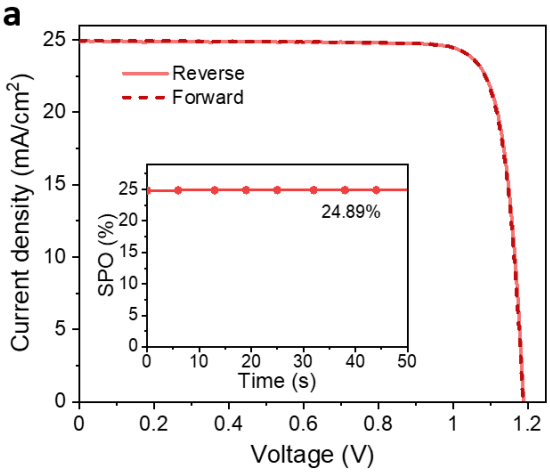

b

Scan	Voc (V)	Jsc (mA/cm^2)	FF (%)	PCE (%)
Forward	1.187	24.953	84.3	24.975
Reverse	1.190	24.888	84.4	24.982

Supplementary Fig. 19. J-V curves with SPO (**a**) and PV parameters (**b**) of a representative device with the best V_{oc} near 1.19 V.

a

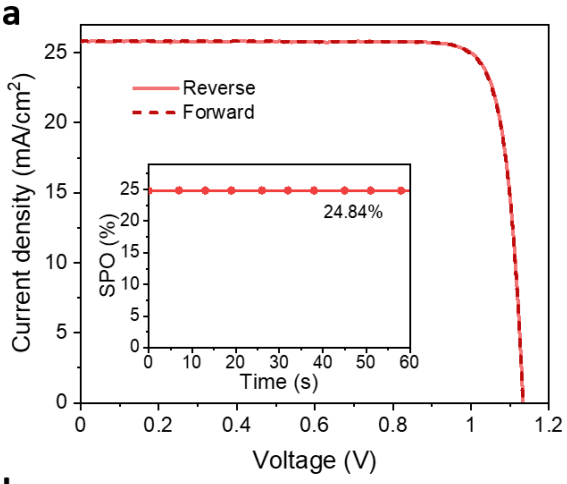

b

Scan	Voc (V)	Jsc (mA/cm²)	FF (%)	PCE (%)
Forward	1.133	25.833	85.3	24.976
Reverse	1.133	25.788	85.7	25.039

Supplementary Fig. 20. J-V curves with SPO (**a**) and PV parameters (**b**) of a representative device with the best FF near 86%.

NREL

Perovskite Cell

Device ID: 1
12:16 PM 1/25/2022
Spectrum: ASTM G173 global

Device temperature: 25.2 ± 0.4 °C
Device area: 0.05825 cm^2 ± 0.5%
Irradiance: 1000.0 W/m^2

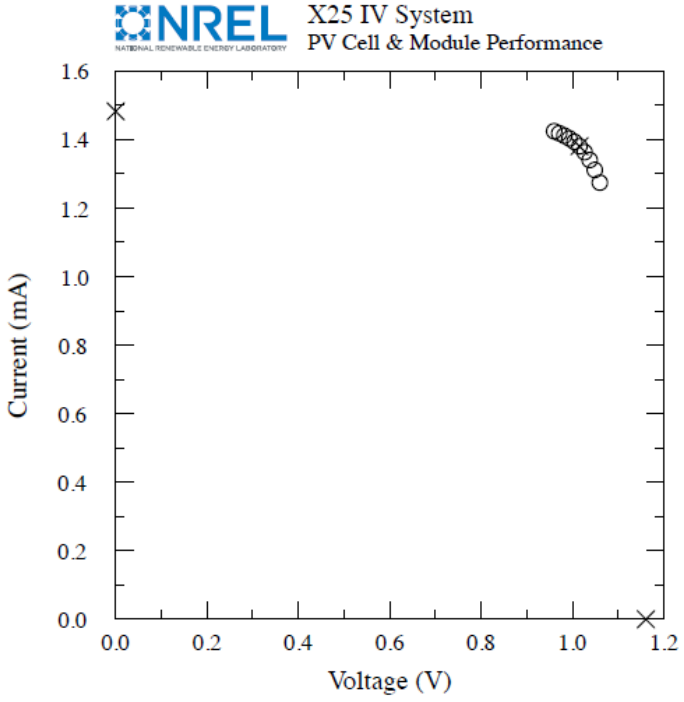

V_{oc} = 1.1607 ± 0.0054 V
I_{sc} = 1.482 ± 0.029 mA
J_{sc} = 25.44 ± 0.51 mA/cm^2
Fill Factor = (81.48 ± 1.86) %

I_{max} = 1.380 ± 0.027 mA
V_{max} = 1.0154 ± 0.0057 V
P_{max} = 1.401 ± 0.028 mW
Efficiency = (24.05 ± 0.48) %

asymptotic IV
Elapsed time: 672 s.

Supplementary Fig. 21. Certification of stabilized photovoltaic (PV) performance of the p-i-n device measured by NREL PV Performance Group. The certification was conducted using the 11-point-Asymptotic P_{max} Scan protocol, where the stabilized asymptotic scans are measured by holding the cell at 11 different voltages near V_{max} until the current change per minute is less than 0.1% before changing to the next voltage point.

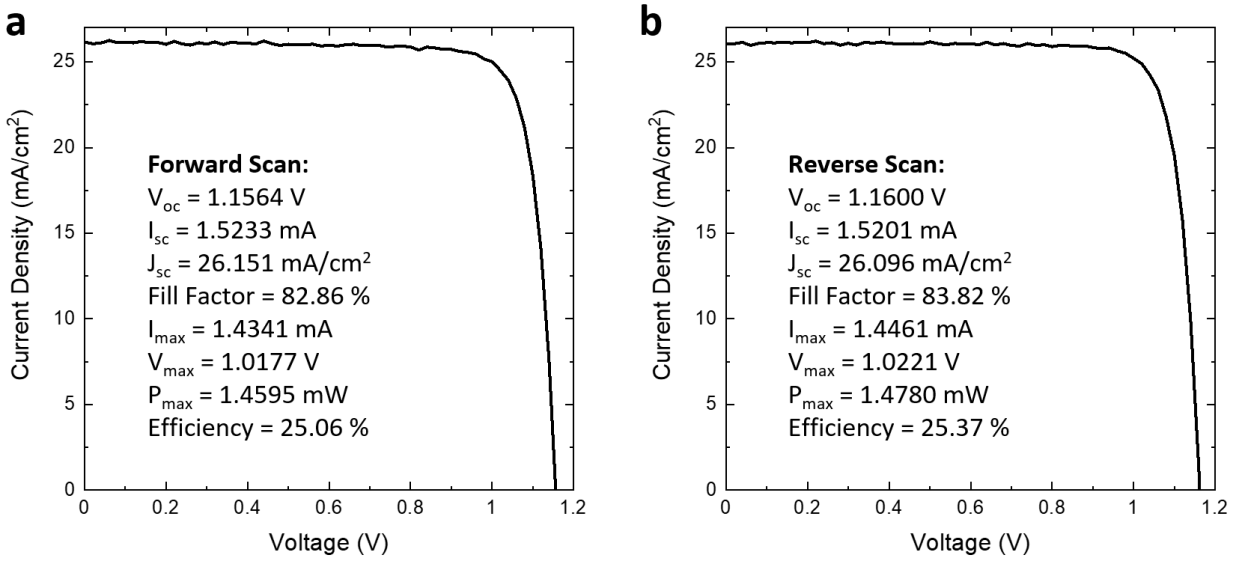

Supplementary Fig. 22. J-V characteristics measured by NREL PV Performance Group on the same device with the certification of the stabilized PV performance as shown in **Supplementary Fig. 21**.

a

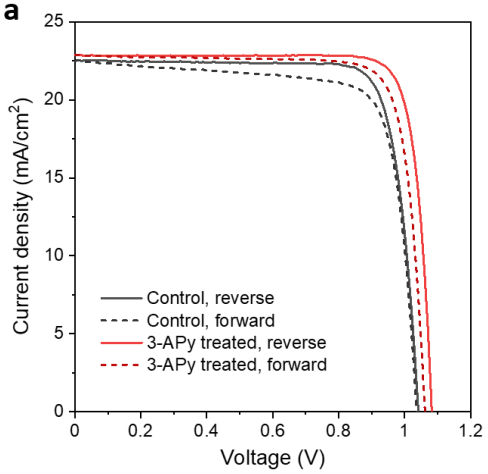

b

	V_{oc} (V)	J_{sc} (mA/cm^2)	FF (%)	PCE (%)
Control, forward	1.04	22.50	77.1	17.99
Control, reverse	1.04	22.48	81.5	19.09
3-APy treated, forward	1.06	22.87	81.7	19.85
3-APy treated, reverse	1.08	22.85	84.4	20.89

Supplementary Fig. 23. J-V curves (**a**) and detailed PV parameters (**b**) of devices without (control) and with 3-APy treatment. The device structure is ITO/MeO-2PACZ/$Cs_{0.13}FA_{0.87}Pb(I_{0.95}Br_{0.05})_3$/$C_{60}$/BCP/Ag. The MA-free $Cs_{0.13}FA_{0.87}Pb(I_{0.95}Br_{0.05})_3$ perovskite has a bandgap of 1.63 eV.

a

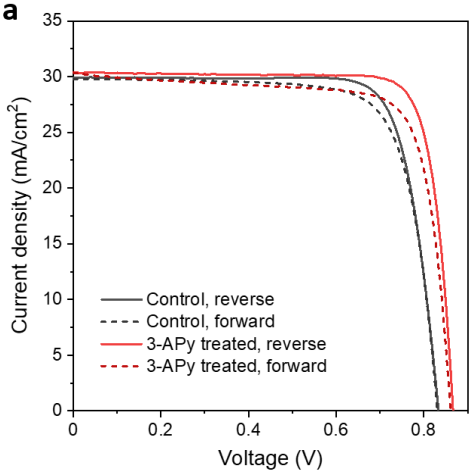

b

	V_{oc} (V)	J_{sc} (mA/cm^2)	FF (%)	PCE (%)
Control, forward	0.83	29.80	75.6	18.72
Control, reverse	0.83	29.92	78.9	19.68
3-APy treated, forward	0.86	30.36	76.7	20.06
3-APy treated, reverse	0.87	30.36	82.7	21.75

Supplementary Fig. 24. J-V curves (**a**) and detailed PV parameters (**b**) of devices without (control) and with 3-APy treatment. The device structure is ITO/PEDOT:PSS/$FA_{0.6}MA_{0.4}Sn_{0.6}Pb_{0.4}I_3$/$C_{60}$/BCP/Ag. The Sn-Pb-based $FA_{0.6}MA_{0.4}Sn_{0.6}Pb_{0.4}I_3$ perovskite has a bandgap of 1.25 eV.

a

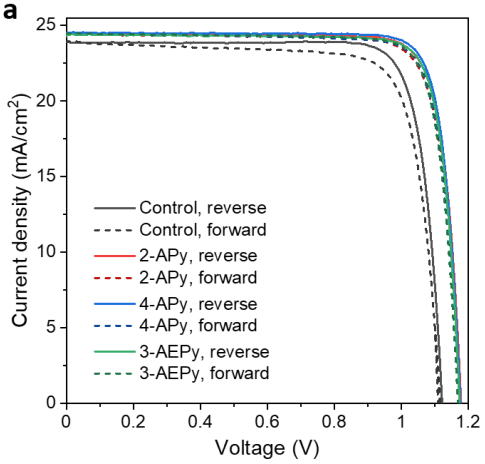

b

	V_{oc} (V)	J_{sc} (mA/cm²)	FF (%)	PCE (%)
Control, forward	1.115	23.98	78.2	20.909
Control, reverse	1.122	23.912	82.4	22.107
2-APy, forward	1.178	24.449	81.9	23.607
2-APy, reverse	1.178	24.449	83.4	24.014
4-APy, forward	1.172	24.433	83.0	23.767
4-APy, reverse	1.176	24.526	84.4	24.361
3-AEPy, forward	1.169	24.488	83.0	23.743
3-AEPy, reverse	1.174	24.402	84.0	24.054

Supplementary Fig. 25. J-V curves (**a**) and PV parameters (**b**) of devices without (control) and with surface treatment using a few different molecules (as indicated), including 2-APy (2-(Aminomethyl)pyridine), 4-APy (4-(Aminomethyl)pyridine), and 3-AEPy (3-(2-aminoethyl)pyridine).

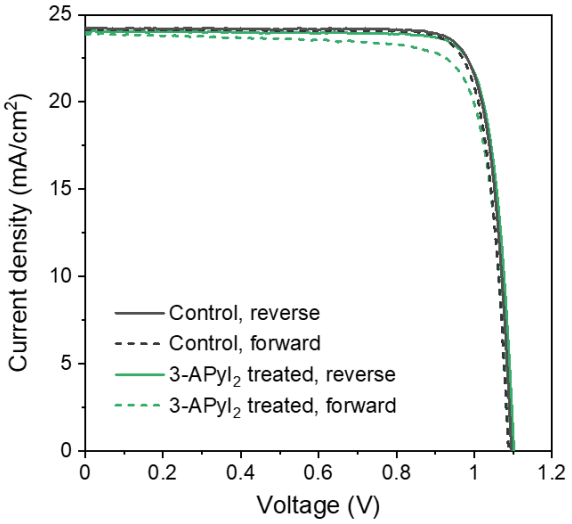

Supplementary Fig. 26. J-V curves of p-i-n cells based on perovskite films without (control) and with (treated) 3-APyI$_2$ surface treatment. 3-APyI$_2$ was dissolved in 2-propanol (IPA).

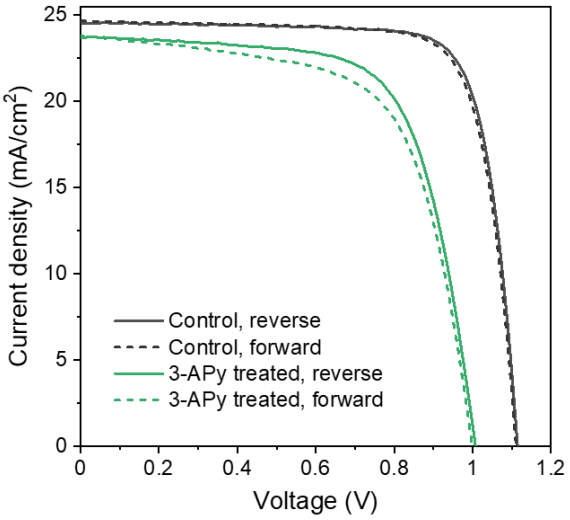

Supplementary Fig. 27. J-V curves of n-i-p cells based on perovskite films without (control) and with (treated) 3-APy surface treatment. The n-i-p device stack is glass/ITO/SnO_2/$FA_{0.93}MA_{0.07}PbI_3$/Spiro-OMeTAD/Au.

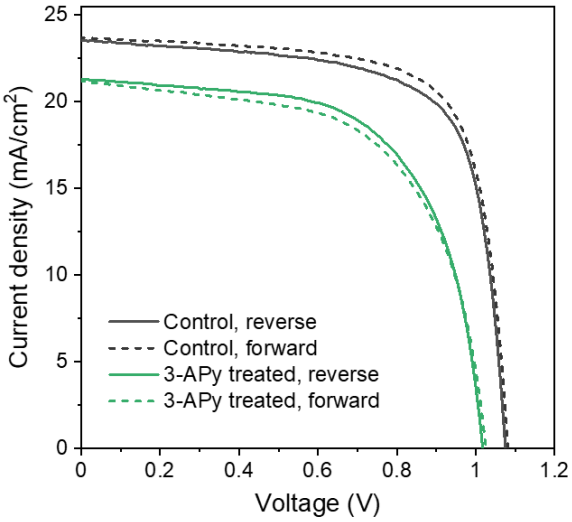

Supplementary Fig. 28. J-V curves of n-i-p cells based on perovskite films without and with 3-APy treatment. Device structure: glass/ITO/SnO_2/$Rb_{0.05}Cs_{0.05}MA_{0.05}FA_{0.85}Pb(I_{0.95}Br_{0.05})_3$/Spiro-OMeTAD/Au.

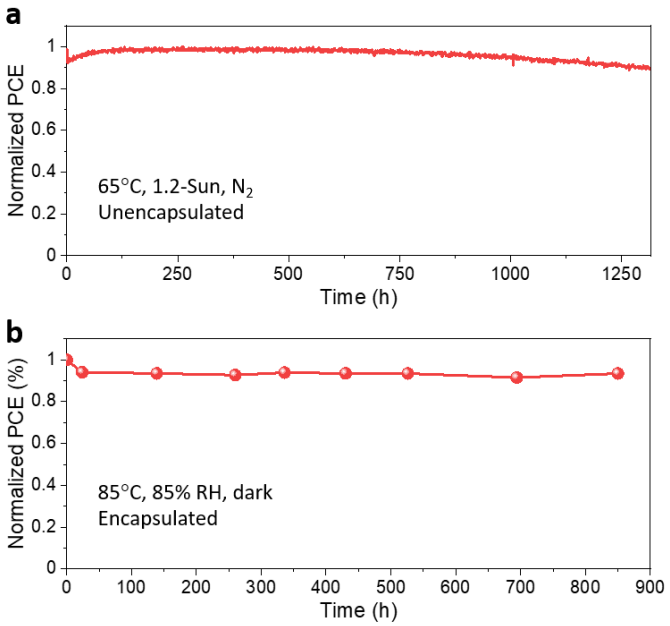

Supplementary Fig. 29. (**a**) Stability evolution of unencapsulated 3-APy-treated target device held at 65°C under continuous 1.2-sun illumination in N_2. After 1315 h, the device retained 90% of its maximum PCE. (**b**) Stability measurements of encapsulated device aged under 85% RH and 85°C in the dark. After 850 h, the device retained ~94% of its maximum PCE.

Supplementary Tables

Supplementary Table 1. Fitting results for TRMC transients shown in Fig. 3c

Sample	A_1	τ_1 (ns)	A_2	τ_2 (µs)	τ_{avg} (µs)
Control	2.585	8.02	48.449	1.75	1.66
Target	16.63	1.95	46.816	2.78	2.06

Note: The average weighted lifetime is extracted using the equation $\tau_{avg} = \frac{A_1\tau_1+A_2\tau_2}{A_1+A_2}$.

Supplementary Table 2. PV parameters of champion control and target (with 3-APy surface treatment) p-i-n PSCs.

Device		J_{sc} (mA/cm^2)	V_{oc} (V)	FF (%)	PCE (%)	SPO (%)
Control	Reverse	25.19	1.12	82.9	23.39	22.85
	Forward	25.35	1.11	78.8	22.18	
Target	Reverse	26.13	1.15	84.6	25.49	25.35
	Forward	26.19	1.15	83.9	25.27	

References

1 Wang, X. *et al.* Perovskite solution aging: what happened and how to inhibit? *Chem* **6**, 1369-1378 (2020).

2 Valenzano, V. *et al.* Methylammonium-formamidinium reactivity in aged organometal halide perovskite inks. *Cell Rep. Phys. Sci.* **2**, 100432 (2021).

3 Van Gompel, W. T. *et al.* Degradation of the formamidinium cation and the quantification of the formamidinium–methylammonium ratio in lead iodide hybrid perovskites by nuclear magnetic resonance spectroscopy. *J. Phys. Chem. C* **122**, 4117-4124 (2018).